Synthesis and characterization of nano-LaFeO3 powders by a soft-chemistry method and corresponding ceramics

Roberto Köferstein, Stefan G Ebbinghaus

Synthesis and characterization of nano-LaFeO₃ powders by a soft-chemistry method and corresponding ceramics

Roberto Köferstein[*] and Stefan G. Ebbinghaus

Institute of Chemistry, Inorganic Chemistry, Martin-Luther-University Halle-Wittenberg, Kurt-Mothes-Strasse 2, 06120 Halle, Germany.

* Corresponding author. Tel.: +49-345-5525630; Fax: +49-345-5527028.
 E-mail address: roberto.koeferstein@chemie.uni-halle.de

Abstract. The preparation of a nano-sized LaFeO₃ powder by a soft-chemistry method using starch as complexing agent is described herein. Phase evolution and development of the specific surface area during the decomposition process of (LaFe)-gels were monitored up to 1000 °C. A phase-pure nano-sized LaFeO₃ powder with a high specific surface area of 25.7 m²/g and a crystallite size of 37 nm was obtained after calcining at 570 °C. TEM investigations reveal a porous powder with particles in the range of 20 to 60 nm. Calcinations to 1000 °C result in crystallite sizes up to 166 nm. Dilatometric measurements of the sintering behaviour show that the beginning of shrinkage of pellets from the nano-sized powder is

downshifted by more than 300 °C compared to coarse-grained mixed-oxide powder. The orthorhombic ⇆ rhombohedral phase transition was observed at 980 °C in DTA measurements for coarse-grained ceramic bodies. The enthalpy change (ΔH) during the phase transition and the thermal expansion coefficient (α_{dil}) for ceramics was determined as 410 J/mol and $11.8 \cdot 10^{-6}$ K^{-1}, respectively. Whereas the enthalpy changes during the phase transition of the nano-sized $LaFeO_3$ powders are ≤ 200 J/mol.

Keywords: *Lanthanum orthoferrite; starch; perovskite; ceramic; sintering; soft-chemistry synthesis*

1. Introduction

Perovskite-related materials based on lanthanum orthoferrite ($LaFeO_3$) are of interest because of their broad applications in advanced technologies. $LaFeO_3$ based materials can be used as catalyst for the decomposition of e.g. hydrocarbons, chlorinated **V**olatile **O**rganic **C**ompounds (VOCs) or by the reaction between NO and CO [1,2,3,4]. They are also candidates as catalysts in heterogeneous Fenton-like reactions for the wet peroxide oxidation of hydrocarbons [5,6] and as photocatalysts [7,8]. Furthermore, doped and undoped lanthanum orthoferrites are applied as sensor materials [9,10,11] and as electrode materials in **S**olid **O**xide **F**uel **C**ells (SOFCs) [12,13,14,15].

$LaFeO_3$ is a ferromagnetic insulator with a Néel temperature of 467 °C [16]. At room temperature it crystallizes in the orthorhombic perovskite structure and exhibits a phase transition to the rhombohedral modification at about 987 °C [17].

The conventional mixed-oxide synthesis of $LaFeO_3$ requires high preparation temperatures and long reaction times. It results in powders with low specific surface area which is

disadvantageous because powders with high specific surface areas can improve the catalytic activity and the densification behaviour of compacts [18,19].

To obtain fine-grained or nano-sized LaFeO$_3$ powders a number of wet-chemical syntheses have been developed such as precursor methods [20,21,22,23], sol-gel and combustion routes [7,24,25]. Nano-sized powders by a microemulsion route were reported by *Giannakas* et al. [26] and *Li* et al. [27]. A microwave-assisted synthesis is described by *Prado-Gonjal* et al. [28]. *Liu* and *Xu* [29] used glucose as a complexing agent in a sol-gel process to produce nano-LaFeO$_3$. Various thermal synthesis of nano-LaFeO$_3$ results in a porous microstructure of the powders [7,20,25,30,31,32,33,34,35].

The aim of this paper is to describe a simple and fast preparation route to obtain nano-sized LaFeO$_3$ powders using starch as a complexation agent and gellant. We use starch because it is an eco friendly and cheap abundant biopolymer. The phase evolution during the decomposition process was monitored by XRD and thermal analysis. For the obtained nanocrystalline LaFeO$_3$ powders the phase transition temperatures and enthalpy changes from the orthorhombic room-temperature to the rhombohedral high-temperature modification were studied. The sintering behaviour and microstructure of resulting LaFeO$_3$ compacts were determined by dilatometry and SEM.

2. Experimental

2.1. Material preparation

La(NO$_3$)$_3$·6H$_2$O (0.006 mol, *Merck*) and Fe(NO$_3$)$_3$·9H$_2$O (0.006 mol, *Merck*) were dissolved in 15 ml water and 2 g soluble starch (*Sigma-Aldrich*) were added. The turbid solution was continuously stirred at room temperature and after 15 min the heating plate was raised to about 120 °C. After about 5 min the solution turned to a highly viscous orange gel. This (LaFe)-gel was calcined in static air at various temperatures up to 1000 °C (heating rate 5 K/min). Calcination at 570 °C for 2 h yielded a nano-sized LaFeO$_3$ powder (**1a**), as described

in detail below. Powder **1a** was mixed with 5 mass% of a saturated aqueous polyvinyl alcohol (PVA) solution as a pressing aid and then the powder was pressed into pellets with a green density of about 1.6–1.7 g/cm^3.

For comparison, a coarse-grained LaFeO$_3$ powder (**2**) was prepared via a semi-conventional mixed-oxide method. La$_2$(C$_2$O$_4$)$_3$·9H$_2$O (*SKW Stickstoffwerke Piesteritz GmbH*) and Fe$_2$O$_3$ (*Sigma-Aldrich*) were ball milled using ZrO$_2$-balls with a molar ratio of 1:1 for 24 h in 30 ml propan-2-ol using ZrO$_2$-balls. After drying, the mixture was calcined at 1200 °C for 8 h (heating rate: 5 K/min) to obtain LaFeO$_3$. Pressing of pellets was carried out as described above. The resulting compacts had a green density of about 4.0–4.1 g/cm^3.

2.2. Characterization

X-ray powder diffraction (XRD) patterns were recorded on a *STOE* STADI MP diffractometer at room temperature using Co−K$_{\alpha 1}$ radiation. Powder patterns were refined with the profile fitting software PowderCell [36]. Crystallite sizes were determined from the XRD line broadening using the Scherrer equation [37] and the integral peak breadth (software suite WinXPOW [38]). The Wilson-equation was used to determine the strain parameter [38,39]. Dilatometric investigations were performed in flowing synthetic air atmosphere (50 ml/min) in a *Setaram* TMA 92-16.18 dilatometer. Simultaneous thermogravimetric (TG) and differential thermoanalytic (DTA) measurements in flowing synthetic air (30 ml/min) were performed using a *Netzsch* STA 449 system. The TG/DTA measurements of the decomposition of the (LaFe)-gel were carried out on a sample preheated at 200 °C for 1 h. The specific surface areas (BET) of the LaFeO$_3$ samples were determined using nitrogen three-point gas physisorption (Nova 1000, *Quantachrome Corporation*). The equivalent BET particle diameters were calculated assuming a spherical or cubic particle shape [40]. ATR-Fourier transformed infrared (FT-IR) spectra were collected at room temperature using a *Bruker* Tensor 27 spectrometer equipped with a diamond ATR unit. TEM images were

recorded with a *Philips* CM20Twin at an electron energy of 200 keV. Scanning electron microscope images were recorded with a *Philips* XL30 ESEM (Environmental Scanning Electron Microscope).

3. Results and discussion

3.1. Powder characterization, TG-DTA, XRD and IR

Heating of the (LaFe)-gel at 200 °C in air for 1 h resulted in a black-brown powder. Simultaneous TG/DTA investigations (heating rate 5 K/min) were carried out on this powder. As shown in Fig. 1a the sample shows a very slight weight loss of about 1.6 % up to 190 °C. At higher temperatures decomposition processes until 610 °C lead to a total weight loss of approximately 31.0 %. During these decomposition processes we observed three strong exothermic DTA signals. The first exothermic process has an onset temperature of 230 °C and the last two signals occur between 310 and 470 °C. These exothermic peaks suggest a self-combustion-like process in which nitrate ions act as an oxidizing agent and starch as fuel. A last sharp weight loss occurs between 610 and 680 °C and is accompanied by a weak exothermic DTA signal with an onset temperature of 617 °C. IR spectroscopy of a sample heated up to 600 °C shows strong CO_3^{2-} absorption bands, whereas XRD pattern shows only an X-ray amorphous product. From this finding the last weight loss can be assigned to the decomposition of carbonate compounds, probably lanthanum carbonate, formed during the combustion of the organic component. This weight loss is linked with the formation of the perovskite crystal lattice as revealed by XRD (see below). The total weight loss up to 900 °C is 35.3 %. XRD investigations of the final ochre coloured product indicated orthorhombic $LaFeO_3$ [41].

TG/DTA measurements in argon atmosphere (Fig. 1b) show a very broad exothermic signal between 80 and 890 °C. The multi-step decomposition process is finished only at 930 °C and lead to a total weight loss of 39.7 %. XRD measurements of the black-brown residue reveal a

mixture of orthorhombic $LaFeO_3$ (main phase), hexagonal La_2O_3 and small amounts of elemental iron [41]. This shows that oxygen is essential for the combustion-like decomposition process to yield phase pure $LaFeO_3$.

Fig. 2 shows the phase evolution during the thermal decomposition of the orange (LaFe)-gel heated in a muffle furnace in static air at various temperatures for 2 h (heating rate 5 K/min). The starting (LaFe)-gel (Fig. 2a) is X-ray amorphous. After calcination at 400 °C a brown X-ray amorphous powder was obtained (Fig. 2b). A powder pattern after a heat treatment at 500 °C hints the presence of La_2O_3 [41] with low crystallinity, while no $LaFeO_3$ was detected (Fig. 2c). At 550 °C besides reflections of La_2O_3 the evolution of $LaFeO_3$ [41] can be observed (Fig. 2d) and a calcination temperature of 570 °C leads to an ochre fluffy phase-pure orthorhombic $LaFeO_3$ powder (**1a**) (Fig. 2d). In contrast to the thermoanalytic results the formation of phase pure $LaFeO_3$ is achieved even below 600 °C, because of the long calcination time of 2 h. With increasing calcination temperature all powders show only reflections according to orthorhombic $LaFeO_3$ (Fig. 2f). The $LaFeO_3$ powder **1a** has a BET specific surface area of 25.7 m^2/g corresponding to an equivalent particle size of 35 nm, which can be considered the average size of the primary particles [42]. The volume-weighted average crystallite size (Scherrer equation) was calculated as 37 nm [37]. According to the Wilson-equation [39] the root-mean-square-strain was found to be 0.003. TEM investigations (Fig. 3) of sample **1a** show a highly agglomerated powder with porous features. The individual particles are mainly in the range of about 20 to 60 nm. Sporadically, we find also particles up to about 100 nm. The pores have diameters of about 15−50 nm.

The XRD pattern of the nano-scaled $LaFeO_3$ powder was refined on the basis of a primitive orthorhombic unit cell (space group: Pbnm) according to *Marezio* and *Dernier* [43]. We calculated the unit cell parameters as a = 555.31 pm, b = 556.29 pm, c = 786.71 pm, V = 243.03·10^6 pm^3. These lattice constants correspond well to previously reported data for pure

LaFeO$_3$ [28,35,44]. The lattice parameters do not significantly change with increasing calcination temperature.

Tab. 1 lists the BET specific surface areas, the equivalent particle sizes and the crystallite sizes of all synthesized LaFeO$_3$ powders. As expected the specific surface area (S_{BET}) decrease with increasing calcination temperature. The logarithmic variation of S_{BET} versus the reciprocal absolute calcination temperature can be fitted by an *Arrhenius* equation [45] as shown in Fig. 4:

$$S_{BET} = A \cdot e^{\frac{-E_A}{RT}} \qquad (1)$$

where A is a pre-exponential factor, E_A is the activation energy for the reduction of the specific surface area, T the absolute temperature and R the universal gas constant. The *Arrhenius* plot given in Fig. 4 shows a positive slop because the specific surface area is reduced with increasing calcination temperature [45]. The activation energy was calculated as $E_A = 28 \pm 2$ kJ/mol. *Andoulsi* et al. [33] found a similar activation energy of $E_A = 20$ kJ/mol during the calcination of nano-LaFeO$_3$ prepared by a polymerizable complex method using ethylene glycol and citric acid. In contrast, the decomposition of a La[Fe(CN)$_6$]·5H$_2$O complex reveals an activation energy for the reduction of the specific surface area of 46 kJ/mol [46].

FT-IR (ATR) spectra of the starting (LaFe)-gel and the corresponding calcination products after heating at 570 °C (powder **1a**) and at 1000 °C (powder **1e**) are shown in Fig. 5. The (LaFe)-gel (Fig. 5a) exhibits a broad band between about 3700 and 2600 cm^{-1} primarily caused by O−H stretching vibrations from water molecules and C−H stretching vibrations from the starch [47]. The O−H bending mode results in an absorption band at 1633 cm^{-1} [48]. Additional bands at 1042 and 1328 cm^{-1} (shoulder at 1406 cm^{-1}) are due to anti-symmetric and symmetric N−O vibrations from the NO$_3^-$ ions [48]. The shoulder at 1406 cm^{-1} represents O−C−H, C−C−H, and C−O−H bending modes from the starch [47]. C−O−H groups cause

C−O stretching vibrations at 1152 cm^{-1}, whereas C−O stretching modes from C−O−C groups appear at 1079 and 1021 cm^{-1} [49].

Calcination at 570 °C (powder **1a**, Fig. 5b) leads to a diminishing of most of the above described structures but also results in a sharp band at 541 cm^{-1}, which can be assigned to a Fe−O stretching vibration and further peaks at 397 and 316 cm^{-1} corresponding to Fe−O−Fe bending or deformation modes [50,51]. Weak adsorptions at about 1481 and 1392 cm^{-1} indicate unidentate adsorbed carbonate groups on the particle surface [20,52,48], which disappear at higher calcination temperatures. Thermal treatment at 1000 °C (powder **1e**) leads to a similar IR spectra, however the intensity of the carbonates bands are strongly reduced (Fig. 5c).

For comparison purposes we also investigated a coarse-grained LaFeO$_3$ powder (**2**) obtained from a semi-conventional mixed-oxide process with calcination at 1200 °C for 8 h. This reference sample has a specific surface area of 2.6 m^2/g and thus an equivalent particle size of 348 nm. The IR spectrum of powder **2** shows the typical Fe−O bands without any detectable carbonate bands (Fig. 5d).

3.2. Sintering behaviour, microstructure and phase transition

Fig. 6 shows non-isothermal dilatometric investigations up to 1500 °C in flowing air of compacts from the nano-powder **1a** and the coarse-grained powder **2**. Since the green compacts **1a** (1.7 g/cm^3) and **2** (4.0 g/cm^3) strongly differ in their densities, the values of the relative shrinkage are not directly comparable. Therefore, from the relative shrinkages the evolution of the relative densities depending on temperature was calculated assuming an isotropic behaviour.

A slight shrinkage of compact **1a** starts from about 750 °C and at 1130 °C the shrinkage increases considerably (Fig. 6). The shrinkage rate reaches a maximum value of -1.19 %/min at 1335 °C as shown in the inset in Fig. 6. Above ≈ 1450 °C we observe only a very slight

length decrease. The calculated relative density reaches 91 % at 1500 °C. In contrast, the shrinkage of the coarse-grained compact **2** starts only at about 1100 °C and a significant increase in shrinkage can be observed above 1200 °C. Two maxima of the shrinkage rate at 1355 °C and at 1406 °C with low rates of -0.20 %/min and -0.18 %/min were found. The densification leads to a relative density of only 74 % up to 1500 °C. The shrinkage rates of both compacts indicate sliding processes as the dominant mechanism, because diffusion processes alone would result in shrinkage rates of less than 0.1 %/min [53,54].

The final bulk densities of ceramic bodies of **1a** and **2** after isothermal sintering at various temperatures with soaking times of 1 and 10 h, respectively, in static air are shown in Fig. 7 (heating-/cooling rate: 5 K/min). The absolute bulk densities of the sintered bodies were calculated from their weight and geometric dimensions. The relative bulk densities were calculated with respect to the crystallographic density of 6.64 g/cm^3 [55]. Coarse-grained powder compacts of **2** show an insufficient densification behaviour. Even after sintering at 1400 °C for 10 h we obtained ceramic bodies with a relative density of only 88 % (Fig. 7). However, compacts from the nano-sized powder **1a** show an improved densification. Sintering at 1300 °C (1 h dwelling time) even leads to dense ceramic bodies with a relative bulk density of 90 %, which is raised to 95 % at 1400−1450 °C (1 h). The microstructures of these ceramic bodies are shown in Fig. 8. The SEM images reveal grain sizes between about 0.6−1.5 µm (1300 °C, Fig. 8a), 12−33 µm (1350 °C), 15−36 µm (1400 °C), and 30−85 µm (1450 °C, Fig. 8b). By raising the sintering time to 10 h we obtained dense ceramics (rel. density ≥ 90 %) at a temperature of 1250 °C as shown in Fig. 7. Up to 1350 °C the relative density increases to 97 %. After soaking time of 10 h the ceramics shows grains of about 0.8−3 µm (1250 °C, Fig. 8c), 2−7µm (1300 °C), and 16−70 µm (1350 °C, Fig. 8d). The improved densification of powder **1a** is a result of its nano-scaled morphology because of the large amount of amorphous or defect-rich grain boundaries, which promote sliding processes [56,54].

Fig. 9 shows DTA investigations of the orthorhombic $\leftrightarrows$ rhombohedral phase transition. The transition temperature was determined by the onset of the DTA signal during the heating phase [57]. The peak area of a DTA signal is proportional to the enthalpy change ΔH (Eq. 2) [58]:

$$\Delta H = k \cdot \frac{A}{m} \qquad (2)$$

where m is the sample mass, A the peak area and k is an instrument-specific proportionality factor. The DTA melting peak of high-purity gold with ΔH = 12.36 kJ/mol (1064 °C) [59] was used to determine the proportionality factor (k) assuming k does not significantly change in the studied temperature interval of the phase transition of $LaFeO_3$.

In the literature phase transition temperatures between 980 °C and 1005 °C have been reported [17,60,61]. DTA measurements on $LaFeO_3$ powders **1c**, **1d** and **1e** (see also Tab. 1) reveal orthorhombic $\leftrightarrows$ rhombohedral phase transition temperatures of 992, 993 and 998 °C (Fig. 9a-c). The corresponding enthalpy changes were calculated as 55, 70 and 200 J/mol, respectively. Investigations on powders **1a** and **1b** show very weak DTA signals, which could not be exactingly analyzed. Fig. 9d represents the DTA curve of a $LaFeO_3$ bulk ceramic body of **1a** sintered at 1300 °C for 1 h. The onset temperature and enthalpy change of the orthorhombic $\leftrightarrows$ rhombohedral phase transition are 980 °C and ΔH = 410 J/mol, respectively. The coarse-grained powder **2** exhibits a similar transition temperature of 989 °C (Fig. 9e). The corresponding enthalpy change of 420 J/mol is not significant different from the bulk ceramic. The similar transition temperatures and enthalpy changes between powder **2** (particle-size: 348 nm) and the ceramic body prepared from the nano-powder **1a** (grain-size: 0.6−1.5 µm) are due the coarse-grained character of both samples. The DTA investigations during the phase transition show that a reduction of the particle size leads to a reduction of the enthalpy change, which has also been observed in other systems [62,63,64]. The reduction of the enthalpy changes with decreasing particle sizes is primarily a surface effect, because of the

increasing surface/volume ratio in small particles as pointed out by various experimental and theoretical studies [65,66,67,68,69,70].

Slightly higher transition temperatures of fine-grained $LaFeO_3$ powders compared to bulk ceramics are also described by *Fossdal* et al. [61]. The magnetic phase transition (not shown) was observed by a broad DTA signal between about 460–480 °C in all samples.

The orthorhombic $\leftrightarrows$ rhombohedral phase transition was also observed by dilatometric measurements on $LaFeO_3$ ceramic bodies (sintered at 1300 and 1400 °C) as it gives rise to a sudden length change of the curve indicating a first-order character of the phase transition (inset in Fig. 9). The transition temperature was determined to 1004 °C at the point of inflection of the measured curve.

The average linear thermal expansion coefficient (α_{dil}) of bulk ceramics was determined by dilatometric measurements using equation 3 [71,72]:

$$\alpha_{dil} = \frac{\Delta L}{L_0 \Delta T} \qquad (3)$$

(L_0 − lengths of the ceramic body at RT, ΔL − length change in the temperature range ΔT). Between 220 and 450 °C an average linear thermal expansion coefficient of $11.8 \cdot 10^{-6}$ K^{-1} was found, which corresponds well with literature data [61].

Conclusion

Nano-sized $LaFeO_3$ powders were synthesized by a soft-chemistry method using starch as a complexing agent and gellant. Calcination of the resulting (LaFe)-gel at 570 °C for 2 h leads to a very fluffy phase-pure $LaFeO_3$ powder (**1a**) with a specific surface area of 25.7 m^2/g and a crystallite size of about 37 nm. TEM images shows a porous powder with particles mainly in the range of 20−60 nm. This nano-sized $LaFeO_3$ powder shows an improved sintering behaviour compared to a sample prepared by semi-conventional solid-state reaction. Dilatometric measurements of compacts from the nano-powder **1a** reveal that the beginning

of the shrinkage is downshifted by more than 300 °C compared with the coarse-grained powder **2**. Dense ceramic bodies (relative density ≥ 90 %) from powder **1a** can be obtained after isothermal sintering at 1250 °C for 10 h. The orthorhombic ⇆ rhombohedral phase transition of LaFeO$_3$ ceramics (grain-sizes: > 1 µm) was found to be 980 °C and is connected with an enthalpy change of ΔH = 410 J/mol. The average linear thermal expansion coefficient between 220 and 450 °C was calculated to be 11.8·10^{-6} K^{-1}. The nano- and fine-grained LaFeO$_3$ powders (crystallite sizes: 37−166 nm) show both slightly higher transition temperatures (992−998 °C) and a decrease of ΔH with decreasing particle-/crystallite size.

Due to its large specific surface area, powder **1a** is a promising candidate for application as catalyst.

Table 1

Variation of S_{BET} and particle-/crystallite size with calcination conditions

Powder	Calcination condition	S_{BET} (m^2/g)	d_{BET} (nm)[1]	d_{cryst} (nm)[2]
1a	570 °C/2h	25.7	35	37
1b	700 °C/2h	17.1	53	54
1c	800 °C/2h	12.0	75	80
1d	900 °C/2h	9.1	99	106
1e	1000 °C/2h	6.5	139	166
2	1200°C/8h	2.6	348	-

1) calculated from the specific surface area
2) volume-weighted average crystallite size (Scherrer equation)
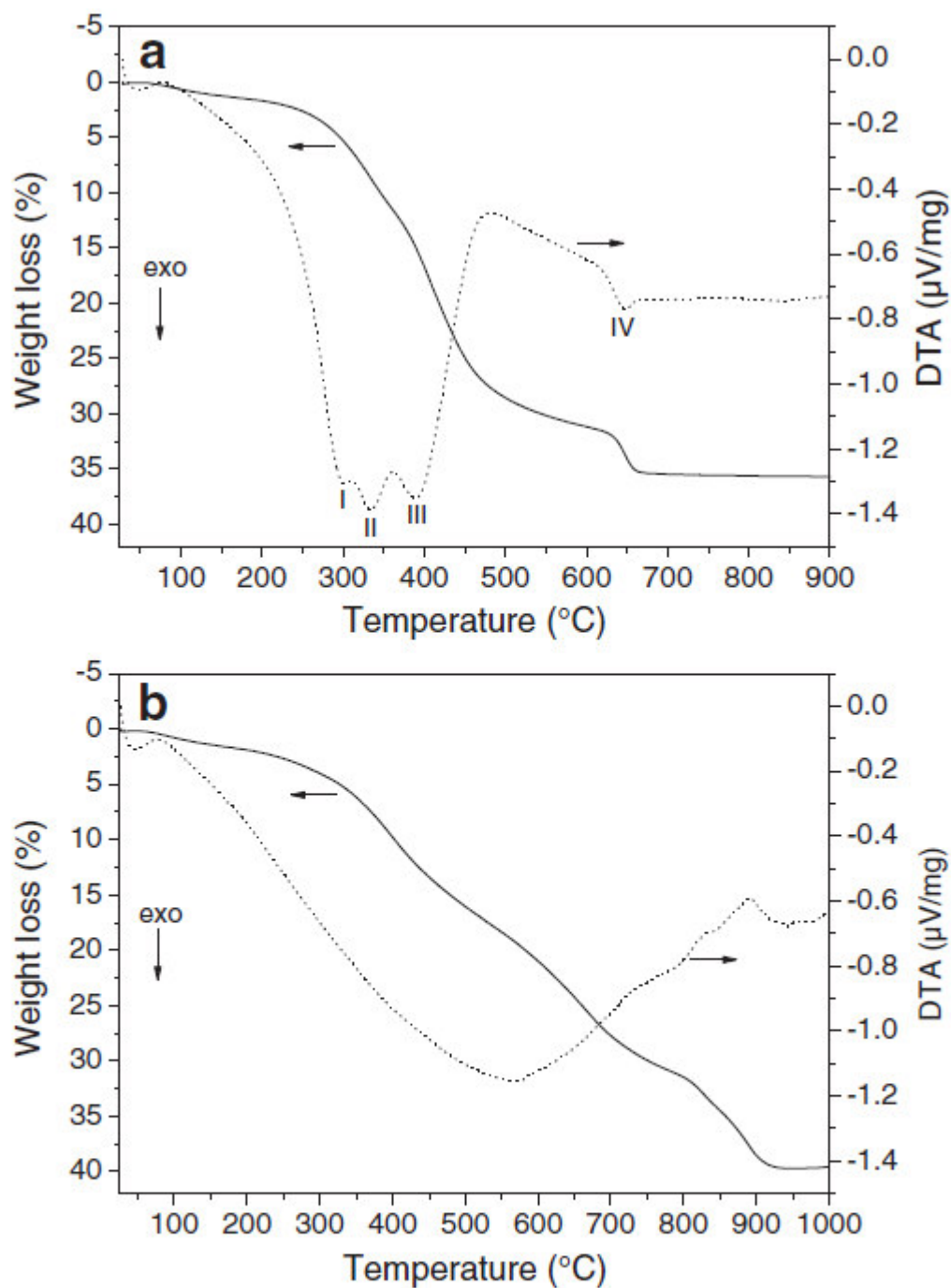
Fig. 1. Simultaneous TG/DTA investigations of a preheated (LaFe)-gel in flowing air (a) and argon atmosphere (b) with heating rates of 5 K/min. In (a) the exothermic processes have maximum peak temperatures of 302 °C (I), 334 °C (II), 388 °C (III), and 649 °C (IV), respectively.
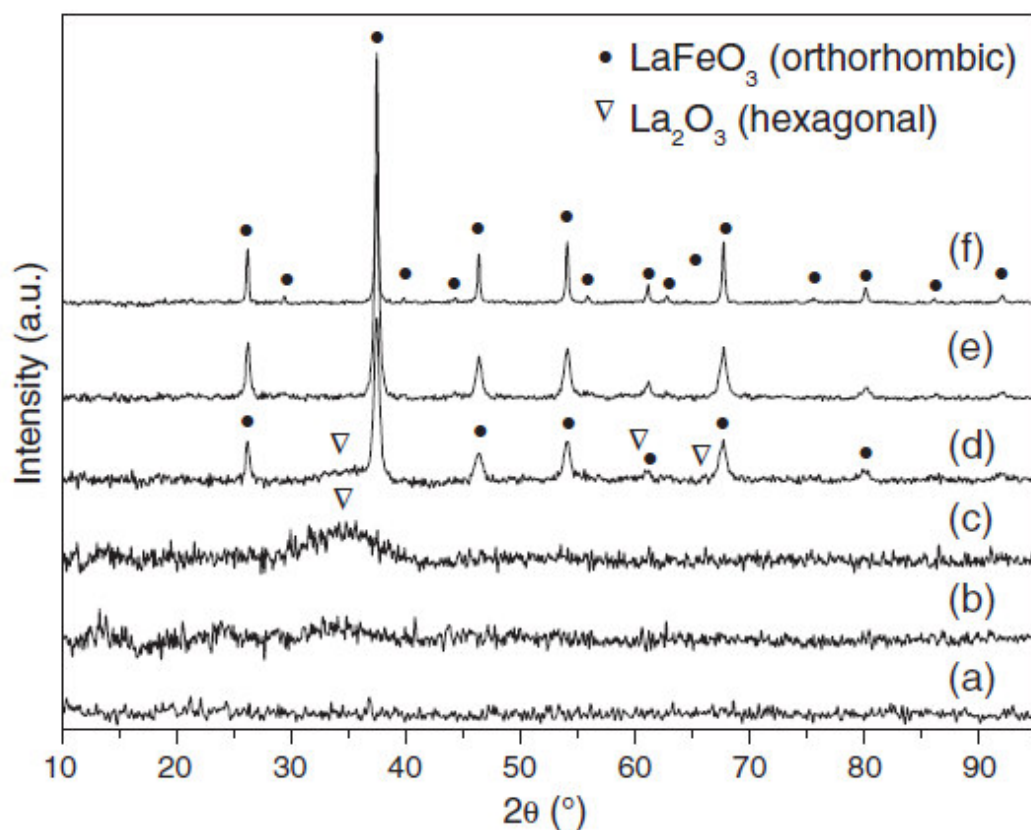
Fig. 2. Room temperature XRD patterns of the (LaFe)-gel (a) and calcination products (b–f) at various temperatures (soaking time 2 h, rate 5 K/min): (b) 400 °C, (c) 500 °C, (d) 550 °C, (e) 570 °C (powder **1a**), and (f) 1000 °C (powder **1e**).
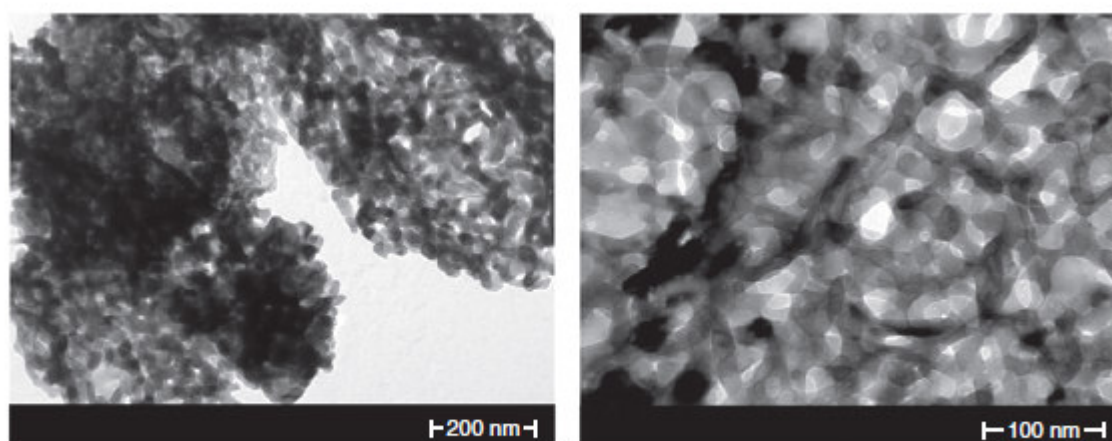

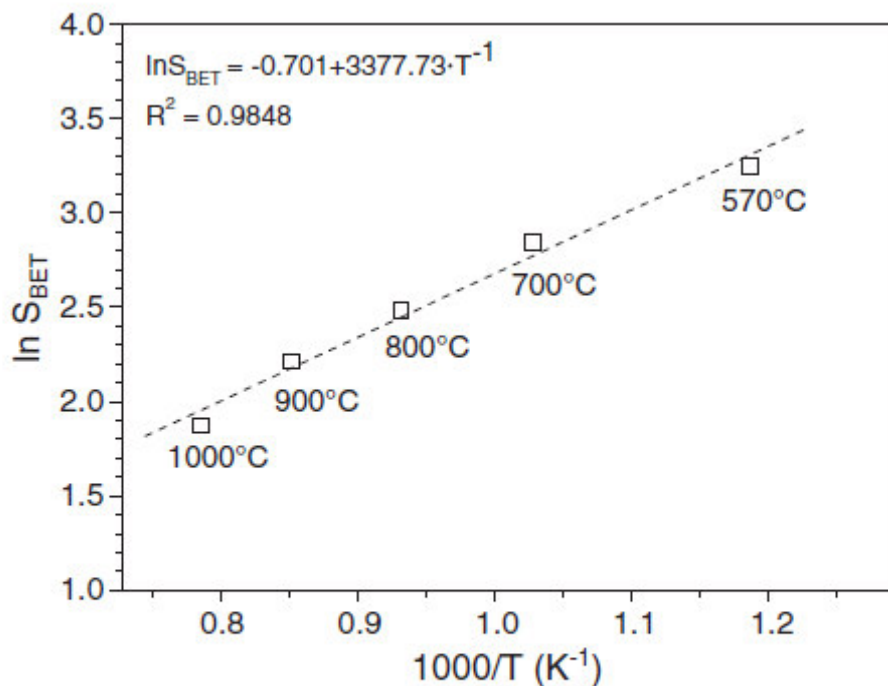**Fig. 3.** TEM images of powder **1a**.

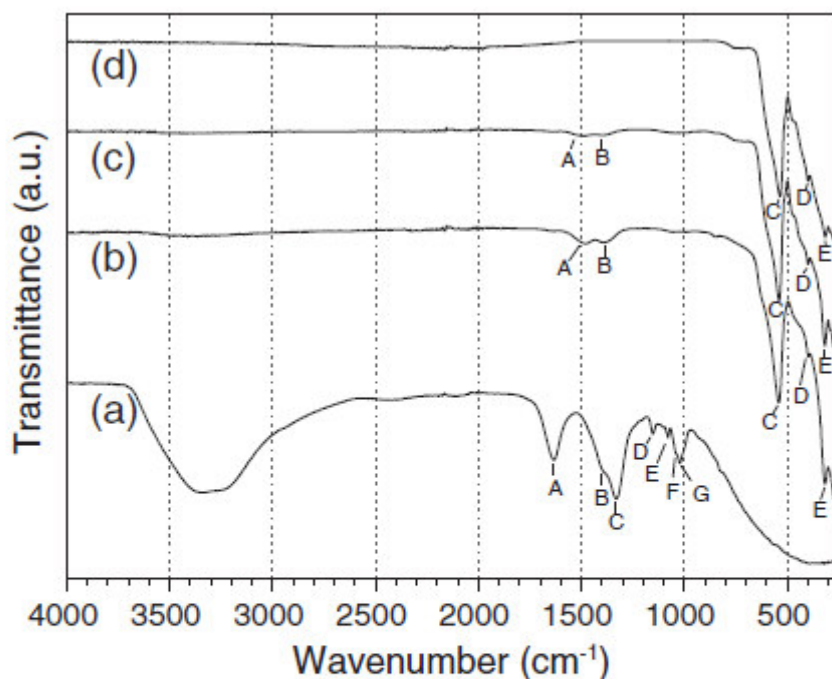**Fig. 4.** Arrhenius plot of the specific surface area versus reciprocal calcination temperature of powders **1a–1e**.

Fig. 5. FT-IR spectra (ATR technique) of (a) (LaFe)-gel, (b) powder **1a**, (c) powder **1e**, and (d) powder **2**. Band positions (cm^{-1}), graph (a): 1633 (A), 1406 (B), 1328 (C), 1152 (D), 1079 (E), 1042 (F), and 1021 (G); graph (b): 1481 (A), 1392 (B), 541 (C), 397 (D), and 316 (E); graph (c): 1486 (A), 1392 (B), 539 (C), 398 (D), and 316 (E); graph (d): 534 (C), 399 (D), and 315 (E).
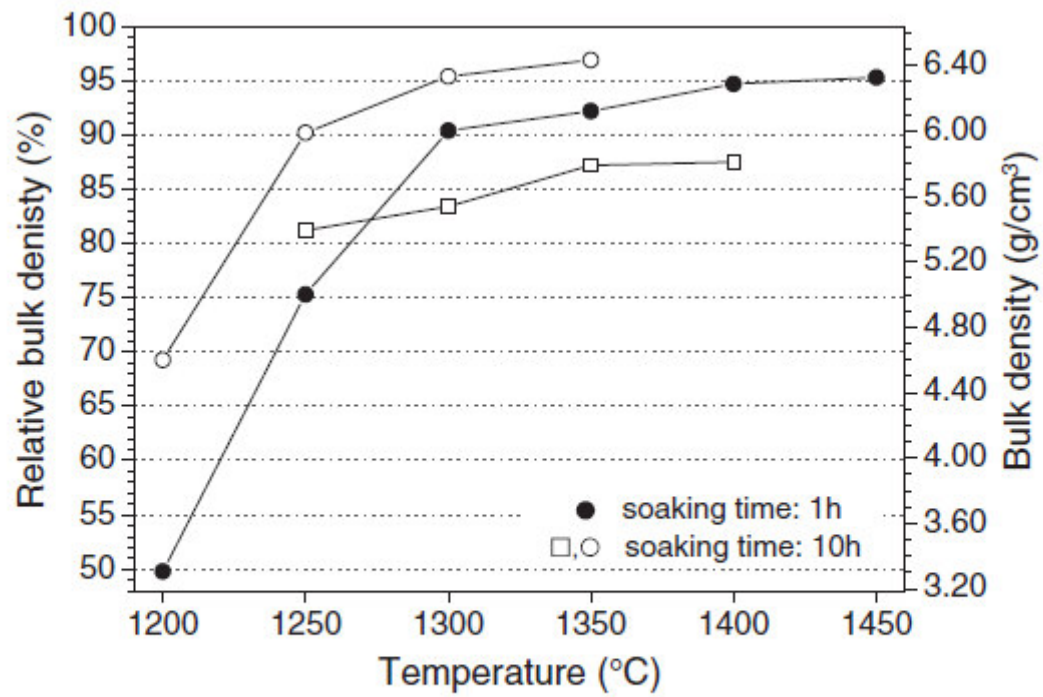
Fig. 7. Final bulk densities versus sintering temperature of ceramic bodies of 1a (○,●) and 2 (□) after soaking times of 1 h and 10 h (heating-/cooling rate: 5 K/min).
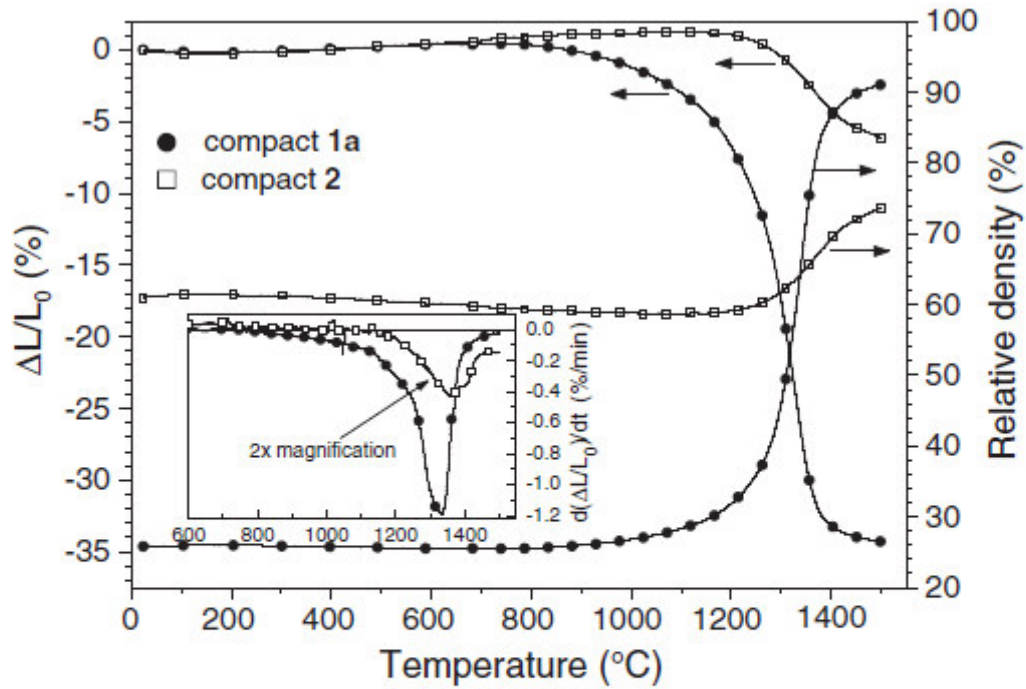
Fig. 6. Non-isothermal dilatometric measurements of green bodies of **1a** and **2** in flowing air (heating rate 5 K/min). Relative densities (in relation to 6.64 g/cm^3) were calculated assuming an isotropic shrinkage behaviour. The inset shows the relative shrinkage rates (d($\Delta L/L_0$)/dt). The green densities were 1.7 g/cm^3 (**1a**) and 4.0 g/cm^3 (**2**), respectively. Every 150th data point is marked by a symbol.
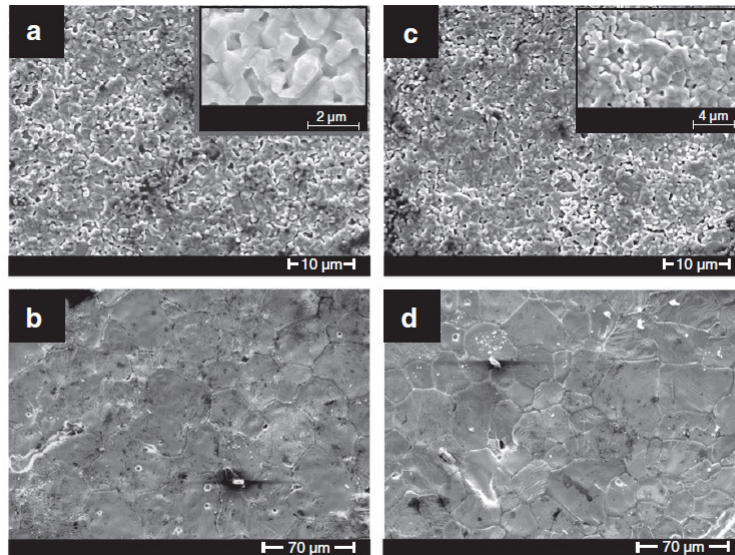

Fig. 8. SEM surface images of ceramic bodies of **1a** after various isothermal sintering conditions (heating rate 5 K/min): a) 1300 °C, 1 h; b) 1450 °C, 1 h; c) 1250 °C, 10 h; and d) 1350 °C, 10 h.
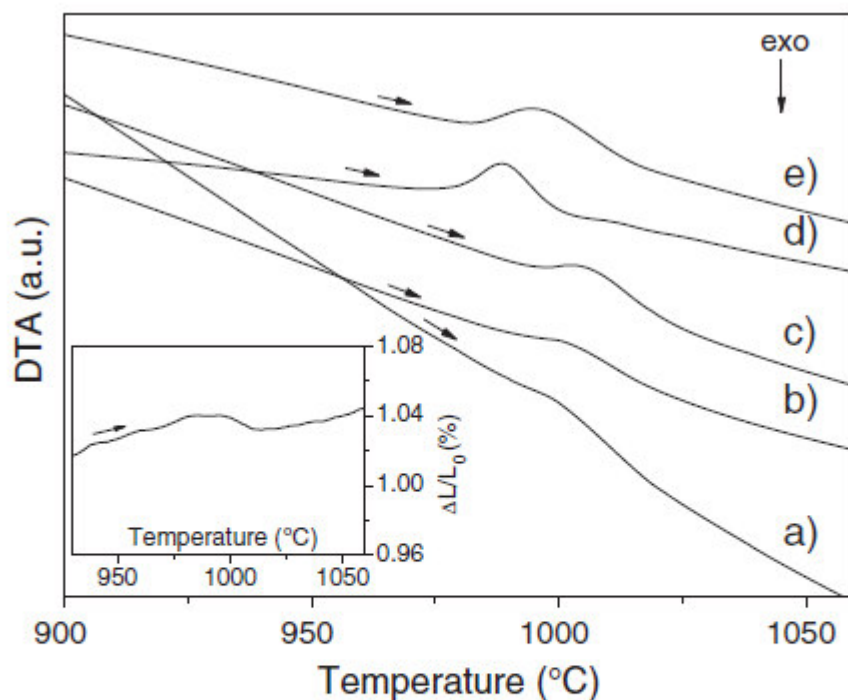
18

Fig. 9. DTA signals in flowing air during the orthorhombic ⇌ rhombohedral phase transition of various $LaFeO_3$ samples (rate 20 K/min). (a) powder 1c, (b) powder 1d, (c) powder 1e, (d) ceramic body of 1a sintered at 1300 °C (1 h), and (e) mixed-oxide powder 2. The inset shows the dilatometric measurement of the expansion of the $LaFeO_3$ ceramics (1300 °C, 1 h) during the phase transition (rate 10 K/min, flowing air).

References

[1]   J. Deng, H. Dai, H. Jiang, L. Zhang, G. Wang, H. He, C.T. Au, *Environ. Sci. Technol.* 44 (2010) 2618–2623.

[2]   Y.-G. Cho, K.-H. Choi, Y.-R. Kim, J.-S. Jung, S.-H. Lee, *Bull. Korean Chem. Soc. 30* (2009) 1368–1372.

[3]   A.E. Giannakas, A.K. Ladavos, P.J. Pomonis, *Appl. Catal. B Environm.* 49 (2004) 147–158.

[4]   A.A. Barresi, D. Mazza, S. Ronchetti, R. Spinicci, M.Vallino, *Stud. Surf. Sci. Catal.* 130 (2000) 1223–1228.

[5]   F. Magalhães, F.C.C. Moura, J.D. Ardisson, R.M. Lago, *Mater. Res.* 11 (2008) 307–312.

[6]   J. Faye, E. Guelou, J. Barrault, J.M. Tatibouet, S. Valange, *Top. Catal.* 52 (2009) 1211–1219

[7]   K.M. Parida, K.H. Reddy, S. Martha, D.P. Das, N. Biswal, *Int. J. Hydrogen. Energ.* 35 (2010) 12161–12168.

[8]   P. Tang, M. Fu, H. Chen, F. Cao, *Mater. Sci. Forum* 694 (2011) 150–154.

[9]   P. Song, H. Quin, L. Zhang, K. An, Z. Lin, J. Hu, M. Jiang, *Sens. Actuators* B104 (2005) 312–316.

[10]   E.N. Armstrong, T. Striker, V. Ramaswamy, J.A. Ruud, E.D. Wachsman, *Sens. Actuators* B158 (2011) 159–170.

[11]   P. Song, Q. Wang, Z. Zhang, Z. Yang, *Sens. Actuators* B147 (2010) 248–254.

[12]   K. Huang, H.Y. Lee, J.B. Goodenough, *J. Electrochem.Soc.* 145 (1998) 3220–3227.

[13]   T.H. Shin, S. Ida, T. Ishihara, *J. Am. Chem. Soc.* 133 (2011) 19399–19407.

[14]   M.-H. Hung, M.V.M. Rao, D.-S. Tsai, *Mater. Chem. Phys.* 101 (2007) 297–302.

[15]   F. Bidrawn, S. Lee, J.M. Vohs, R.J. Gorte, *J. Electrochem. Soc.* 155 (2008) B660–B665.

[16]   J.W. Seo, E.E. Fullerton, F. Nolting, A. Scholl, J. Fompeyrine, J.-P. Locquet, *J. Phys. Condens. Matter* 20 (2008) 264014.

[17]   S. Geller, P.M. Raccah, *Phys. Rev.* B2 (1970) 1167–1172.

[18]   R. Köferstein, L. Jäger, M. Zenkner, S.G. Ebbinghaus, *J. Eur. Ceram. Soc.* 29 (2009) 2317–2324.

[19]   A.V. Orlov, O.A. Shlyakhtin, A.L. Vinokurov, A.V. Knotko, Y.D. Tretyakov, *Inorg. Mater.* 41 (2005) 1194−1200.

[20]   E. Traversa, P. Nunziante, M. Sakamoto, Y. Sadaoka, M.C. Carotta, G. Martinelli, *J. Mater. Res.* 13 (1998) 1335−1344.

[21]   G. Shabbir, A.H. Qureshi, K. Saeed, *Mater. Lett.* 60 (2006) 3706–3709.

[22]   H. Xu, X. Hu, L. Zhang, *Cryst. Growth Des.* 8 (2008) 2061–2065.

[23]   X. Li, H. Zhang, M. Zhao, S. Li, B. Xu, *J. Mater. Chem.* 2 (1992) 253–254.

[24]   S. Li, L. Jing, W. Fu, L. Yang, B. Xin, H. Fu, *Mater. Res. Bull.* 42 (2007) 203–212.

[25]   M.B. Bellakki, B.J. Kelly, V. Manivannan, *J. Alloys Compd.* 489 (2010) 64−71.

[26]   F.-T Li, Y. Liu, R.-H. Liu, Z.-M. Sun, D.-S. Zhao, C.-G. Kou, *Mater. Lett.* 64 (2010) 223–225.

[27]   A.E. Giannakas, A.K. Ladavos, P.J. Pomonis, *Appl. Catal. B-Environ.* 49 (2004) 147–158.

[28]   J. Prado-Gonjal, A.M. Arevalo-Lopez, E. Mora, *Mater. Res. Bull.* 46 (2011) 222–230.

[29]   T. Liu, Y. Xu, *Mater. Chem. Phys.* 129 (2011) 1047–1050.

[30]   F.-T Li, Y. Liu, Z.-M. Sun, R.-H. Liu, C.-G Kou, Y. Zhao, D.-S Zhao, *Mater. Lett.* 65 (2011) 406–408.

[31]   M.B. Bellakki, V. Manivannan, J. Das, *Mater. Res. Bull.* 44 (2009) 1522−1527.

[32]   H. Shen, G. Cheng, A. Wu, J. Xu, J. Zhao, *Phys. Status Solidi* A206 (2009) 1420−1424.

[33]   R. Andoulsi, K. Horchani-Naifer, M. Férid, *Ceramica* 58 (2012) 126−130.

[34]   Y. Wang, J. Zhu, L. Zhang, X. Yang, L. Lu, X. Wang, *Mater. Lett.* 60 (2006) 1767−1770.

[35]   J. Wang, Q. Liu, D. Xue, F. Li, *J. Mater. Sci. Lett.* 21 (2002) 1059−1062.

[36]   W. Kraus, G. Nolze, Powder Diffr. 13 (1998) 256–259.

[37]   Th.H. De Keilser, E.J. Mittermeijer, H.C.E Rozendaal, *J. Appl. Cryst.* 16 (1983) 309−316.

[38]   Program WinXPOW v1.06, Stoe & Cie GmbH, Darmstadt (1999).

[39]   A.R. Stokes, A.J.C. Wilson, *Proc. Phys. Soc.* 56 (1944) 174−181.

[40]   V.D. Allred, S.R. Buxton, J.P. McBride, *J. Phys. Chem.* 61 (1957) 117−120.

[41]   PDF 2 (International Centre for Diffraction Data, Pennsylvania) 2001, $LaFeO_3$ [74-2203], La_2O_3 [73-2141], Fe [85-1410].

[42]   M.T. Buscaglia, M. Bassoli, V. Buscaglia, R. Alessio, *J. Am. Ceram. Soc.* 88 (2005) 2374–2379.

[43]   M. Marezio and P.D. Dernier, *Mater. Res Bull.* 6 (1971) 23−30.

[44]   M. Kumar, S. Srikanth, B. Ravikumar, T.C. Alex, S.K. Das, *Mater. Chem. Phys.* 113 (2009) 803–815.

[45]   G.E. Shter, A.R. Schwartzman, G.S. Grader, *Appl. Supercond.* 3 (1995) 543−550.

[46]   S. Nakayama, *J. Mater. Sci.* 36 (2001) 5643–5648.

[47]   P.R. Changa, P. Zheng, B. Liu, D.P. Anderson, J. Yu, X. Ma, *J. Hazard. Mater.* 186 (2011) 2144−2150.

[48]   K. Nakamoto, *Infrared and Raman Spectra of Inorganic and Coordination Compounds.* John Wiley & Sons, USA, 1986.

[49]   J.M. Fang, P.A. Fowler, J. Tomkinson, C.A.S. Hill, *Carbohydr. Polym.* 47 (2002) 245−252.

[50]   G.V. Subba Rao, C.N.R. Rao, J.R. Ferraro, *Appl. Spectrosc.* 24 (1970) 436−445.

[51]   M.A. Ahmed, R. Seoudi, S.I. El-dek, *J. Mol. Struct.* 754 (2005) 41–44.

[52]   H.-M. Zhang, Y. Teraoka, N. Yamazoe, *Chem. Lett.* (1987) 665−668.

[53]   R. Köferstein, L. Jäger, M. Zenkner, S.G. Ebbinghaus, *J. Eur. Ceram. Soc.* 29 (2009) 2317−2324.

[54]   W. Schatt, *Sintervorgänge.* VDI-Verlag, Düsseldorf, 1992, pp. 78–100.

[55]   L. Prado-Gonjal, A.M. Arevalo-Lopez, E. Moran, *Mater. Res. Bull.* 46 (2011) 222−230.

[56]   W. Schatt, *Z. Metallkde.* 80 (1989) 809−816.

[57]   H. K. Cammenga and M. Epple, *Angew. Chem.* 107 (1995) 1284−1301.

[58]   M.E. Brown, *Introduction to Thermal Analysis.* Chapman and Hall, New York, 1988.

[59]   J.E. Callanan, *J. Thermal. Anal.* 45 (1995) 359−368.

[60]   T. Ohzeki, T. Hashimoto, K. Shozugawa, M. Matsuo, *Solid State Ionics* 181 (2010) 1771–1782.

[61]   A. Fossdal, M. Menon, I. Wærnhus, K. Wiik, M.-A. Einarsrud, T. Grande, *J. Am. Ceram. Soc.,* 87 (2004) 1952–1958.

[62]   R. Köferstein, L. Jäger, M. Zenkner, S.G. Ebbinghaus, *Mater. Chem. Phys.* 119 (2010) 118–122.

[63]   W.L. Zhong, B. Jiang, P. L. Zhang, J.M. Ma, H.M. Cheng, Z.H. Yang, L.X. Li, *J. Phys.: Condens. Matter.* 5 (1993) 2619–2624.

[64]   X. M. Chen, G.T. Fei, K. Zheng, *J. Phys.: Condens. Matter* 21 (2009) 245403.

[65]   J. Sun, S.L. Simon, *Thermochim. Acta* 463 (2007) 32–40.

[66]   L.H. Liang, M. Zhao, Q. Jiang, *J. Mater. Sci. Lett.* 21 (2002) 1843–1845.

[67]   M. Zhang, M.Yu. Efremov, F. Schiettekatte, E.A. Olson, A.T. Kwan, S.L. Lai, T. Wisleder, J.E. Greene, L.H. Allen, *Phys. Rev.* B62 (2000) 10548–10557.

[68]   R. Lipowsky, *Ferroelectrics* 73 (1987) 69–81.

[69]   L. H. Liang, G.W. Yang, B. Li, *J. Phys. Chem.* B109 (2005) 16081–16083.

[70]   M. Kuwabara, H. Matsuda, N. Kurata, E. Matsuyama, *J. Am. Ceram. Soc.* 80 (1997) 2590–2596.

[71]   J.D James, J.A Spittle, S.G.R Brown, R.W Evans, *Meas. Sci. Technol.* 12 (2001) R1–R15.

[72] W.F. Hemminger and H.K. Cammenga, *Methoden der Thermischen Analyse.* Springer-Verlag, Berlin-Heidelberg, 1989.